Effect of cooling regime on structure of entropy-stabilized oxides (MgNiCoCuZn)O

© S.B. Vakhrushev[1], A.A. Naberezhnov[1,¶], S.V. Sumnikov[2], Varatharaja Nallathambi[3,4], Lalith Kumar Bhaskar[3,4], Ravi Kumar[3,4]

[1] Ioffe Institute,
St. Petersburg, Russia
[2] Frank Neutron Physics Laboratory, Joint Nuclear Research Institute,
Dubna, Russia
[3] Laboratory for High Performance Ceramics, Department of Metallurgical and Materials Engineering,
Indian Institute of Technology Madras (IIT Madras),
Chennai, 600036, India
[4] Ceramic Technologies Group, Centre of Excellence in Materials and Manufacturing for Futuristic Mobility,
Indian Institute of Technology, Madras (IIT Madras),
Chennai 600036, India

¶ E-mail: alex.nabereznov@mail.ioffe.ru

The effect of various cooling regimes on the evolution of the crystal structure of entropy- stabilized oxides (MgNiCoCuZn)O has been studied using a high-resolution time-of-flight neutron Fourier diffractometer. It has been established that cooling in a furnace at a rate of 1, 2, and 5 K/min leads not only to the segragation of a part of copper oxide into a separate phase, but also to nanostructuring of both the main matrix and CuO. The characteristic sizes of the formed nanoparticles are determined. It is shown that the expected rhombohedral or tetragonal distortions due to the possible Jahn-Teller effect are not observed in these samples.

Keywords: entropy-stabilized oxides, neutron diffraction, crystal structure, profile analysis.

1. Introduction

The concept of creation of fundamentally new functional materials, later called high-entropy alloys (HEA), was developed at the end of 20th−early 21st century in the works of [1,2] and was initially applied to multicomponent metal alloys, containing 5 or more base metals with the content in the range from 5 to 35%. A number of alloys with very promising properties for practical applications have been created using this approach [2,3], and existing approaches to describing the properties and characteristics of HEA, as well as the prospects for the development of this technology, are well presented in the review [4]. The success of this concept stimulated the expansion of the class of objects to create other high-entropy materials, and the next step was the synthesis of structures based on a mixture of MgO, CoO, NiO, CuO and ZnO oxides: they were later called entropy-stabilized oxides (ESO, the abbreviation HEO is often used — high-entropy oxides) [5]. It was shown that a single-phase solid solution with a rock salt structure and with a random distribution of cations is formed only with the equimolar composition of this mixture (MgCoNiCuZn)O. It should be noted here that there are no solid solutions between any of the initial oxides in this mixture. The authors also argued that it is the configuration disorder that

leads to the stabilization of the phase state of this solid solution. Later, this point of view about the uniqueness of this stabilization mechanism was somewhat corrected in [6], which showed that attention should also be paid to the values of mutual solubility of oxides in the synthesis of ESO type materials. The approach developed to create ESO turned out to be very fruitful, and later similar materials were created based on carbides [7], sulfides [8], nitrides [9] and diborides [10]. As for the compounds of the ESO class, their macroscopic physical properties have been studied in detail in recent years, and the materials themselves are already widely used. For example, it was found in [11] that dielectric constant ε has a value of the order of 1000 (and more) in the frequency range from 100 Hz to 2.3 MHz in ESO-based materials, while the value ε remains practically frequency-independent, and the dielectric losses do not exceed 0.01. A great efficiency of using these materials at high temperatures as a catalyst for the oxidation of CO was shown in [12]. ESO membranes [13] have proven to be highly effective in cleaning water from dyes. Ceramics made of high-entropy oxides can have (for example, when doped with lithium) high superionic conductivity [14], they can thermochemically decompose water [15], have a strong potential for use as thermoelectric materials [16]. It was also found that the change of the CuO content in the initial

Table 1. Specimen characteristics

Number	Designation	Specimen Description	Note
S1	ESO 5C	Single-phase stabilized (MgNiCoCuZn)O, natural cooling („quenching") in air	
S2	ESO SC-5	Obtained on cooling to room temperature the temperature in the oven at a rate of 5°C/min	Contains 5.4 wt.% CuO
S3	ESO SC-2	Obtained on cooling to room temperature the temperature in the oven at a rate of 2°C/min	Contains 8.2 wt.% CuO
S4	ESO SC-1	Obtained on cooling to room temperature temperatures in the oven at a rate of 1°C/min	Contains 12.3 wt.% CuO
S5	ESO 4C	Single-phase (MgNiCoZn)O	Without CuO

material during the synthesis has the strongest effect on the macroscopic properties and structure of ESO [17]. In addition, detailed X-ray diffraction studies of specimens $(MnCoNiZn)_{1-x}Cu_xO$ ($x = 0.16$, 0.18, 0.2, 0.22, 0.24, 0.26, 0.28) under different heating and cooling conditions showed a significant evolution of the crystal structure of these materials itself while the cubic symmetry is generally maintained. It was suggested by [17,18] that the observed anomalies may be caused by local distortions of the oxygen sublattice due to the Jan-Teller effect, which is characteristic for Cu^{2+} ions in an octahedral environment. These distortions should be either tetragonal or rhombohedral, and then the corresponding splitting of Bragg peaks should appear on diffraction patterns. At the same time, the authors did not directly observe such splitting, although the results of EPR data indicate that some distortions of octahedra CuO_6 exist [17]. Possibly, this is attributable to the insufficient resolution of the diffractometer used.

The purpose of this work was to search for possible distortions of the crystal structure and to collect information about the impact of different cooling modes the structure of ESO specimens based on the analysis of neutron scattering diffraction patterns acquired using high-resolution Fourier diffractometer HRFD (JINR, FLNP, Dubna) [19,20].

2. Specimens and experimental methods

The specimens were made by the Indian Institute of Technology Madras (IIT Madras), solution combustion synthesis (SCS) technology is described in the article [21]. 5 types of specimens S1−S5 were used for measurements (Table 1). Specimens S1−S4 were made using the same technology and differed only in the cooling mode, specimen S5 was made using the same technology, but did not contain CuO. The initial (after synthesis) ceramics for the preparation of specimens S1−S4 had the following composition according to the results of energy-dispersive X-ray spectroscopy — EDS [21] (in at.%): O — 45.4 (3.5), Mg — 11.4 (1.4), Ni — 10.9 (0.8), Co — 11.1 (0.7), Cu — 10.8 (0.9),

Zn — 10.3 (0.8). Composition the specimen S5 meets the equimolarity condition. A part of copper oxide was released (Table 1) when the specimens S2−S4 were cooled, and the specimens became two-phase: distinct peaks corresponding to tenorite phase (CuO) were observed in addition to the main phase corresponding to the structure of rock salt (etc., group $Fm\bar{3}m$) [21]. The S5 specimen, which does not contain copper ions, was used as a reference, since structure distortions associated with the Jan-Teller effect should not be expected in it.

Further, powder specimens were made from the produced ceramics and they were used to perform neutron diffraction studies at room temperature using a high-resolution time-of-flight Fourier diffractometer HRFD. The measurement time of each specimen was 8 hours. The operating range for interplanar spacing was from $d = 0.6$ Å to 2.4 Å, the resolution of the diffractometer FWHM/d (here FWHM — full width at half maximum, d — the interplanar spacing) ranged from 0.0021 at $d = 0.6$ Å to 0.0017 at $d = 2.4$ Å. The diffractometer was calibrated using a standard specimen Al_2O_3. Diffraction patterns were treated using the Rietveld method (FullProf package).

3. Results and discussion

Figure 1 shows the diffraction pattern (dots) and the fitting results for the specimen S5. The positions of the peaks correspond well to the structure of rock salt (pr. Fm-3m group), no additional peaks were detected. The width of the peaks is almost completely determined by the instrumental resolution and we did not find any additional broadening in the experiment. The R-factor is 2.49, which indicates a good fit quality.

Elastic peaks of equimolar specimen S1 become slightly wider than the instrumental resolution, and a sharp increase of the width of all peaks of specimens S2−S4 is observed: Figure 2 shows the evolution of the line shapes of the most intense elastic peaks (200), (220) and (222) of specimens S1−S5, with the greatest broadening of reflection

Table 2. Cell parameters for all ESO specimens and width values

Specimen	Parameter cells a, Å	σ (200), Å	σ (220), Å	σ (222), Å
S1 ESO 5C	4.2378(2)	0.00273(3)	0.00165(2)	0.00120(2)
S2 ESO SC-5	4.2350(3)	0.00545(5)	0.00296(4)	0.00178(2)
S3 ESO SC-2	4.2347(2)	0.00430(5)	0.00234(3)	0.00155(2)
S4 ESO SC-1	4.2344(4)	0.00484(5)	0.00272(3)	0.00183(2)
S5 ESO 4C	4.2341(1)	0.00164(1)	0.00118(1)	0.000986(6)
The value σ_0 expected from the function diffractometer resolutions		0.00152(1)	0.00117(1)	0.000978(3)

(standard deviations σ) for elastic peaks (200), (220) and (222).

(200) (Fig. 2, d shows the intensity distributions of this peak for all the specimens studied, normalized to the corresponding maxima). All elastic peaks on diffractograms correspond to the structure of rock salt: the R-factor ranges from 4.5 to 7.4. No other phases are observed, which is surprising, since distinct peaks from the tenorite structure, i.e. CuO copper oxide [5,17,21] were present in X-ray diffraction studies of S2−S4 specimens. Question „Why is the contribution from the tenorite not observed?" will be discussed later. Note that all distributions are well described by the Gaussian function. The values of the lattice cell parameters and peak widths (in this case, the standard deviation parameters σ) given in Table 2 were obtained using the fitting.

It is clearly seen from the data given in Table 2 that a decrease of the copper oxide content in the ESO structure does not only increases the widths of elastic peaks, but it also to reduces the size of the lattice cell. The observed increase of the width of elastic peaks can be caused by several reasons, one of which may be the appearance of weak tetragonal, corresponding to the I4/mmm group,
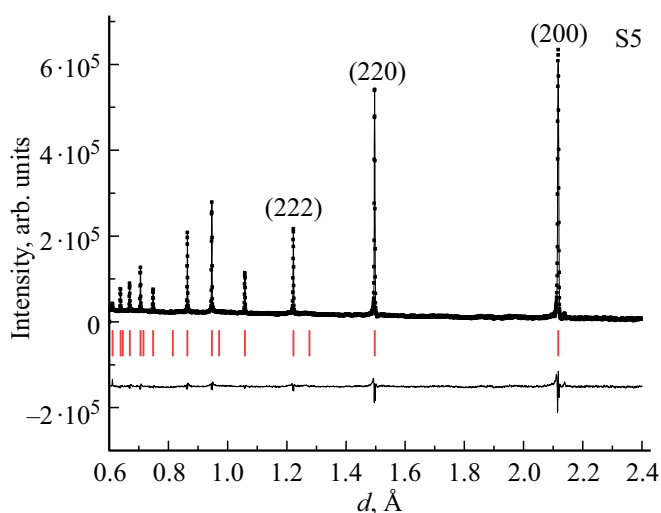
or rhombohedral distortions (R-3m group, etc.) of the structure due to the Jan-Teller effect, as already mentioned above. In principle, the appearance of such distortions should lead to splitting of peaks, as shown in [17]. In case of tetragonal distortions, the reflections (200) and (220) of the cubic phase should split into peaks $(110)_t + (002)_t$ and $(200)_t + (112)_t$ (index t means that the reflection belongs to the tetragonal phase), respectively, and the peak (222) should not change. In case of rhombohedral distortions, the peak (200) of the cubic structure should not change, and the peak (220) should split. This should lead to distortion of the shape of the line of these peaks (to the appearance of asymmetry), if these distortions are not too small to be observed in our experiment. No obvious changes of the shape of the peaks are visible according to the data shown in Fig. 2, $a-d$. The simulation showed that the change of the lattice parameter does not exceed the value of $\sigma_0/2$ even for the most strongly widened peak (200), thus the parameter of cell a does not change by more than 0.0007 Å, i.e. which significantly less than the instrumental resolution and cannot be detected in this experiment. Moreover, the observed shape of the line for reflexes (200), (220) and (222) cannot be satisfactorily described using the assumption that there are two phases: cubic and tetragonal, cubic and rhombohedral, or tetragonal and rhombohedral. Thus, the mechanism of broadening of elastic reflections due to tetragonal or rhombohedral distortions should be considered as unconvincing.

The dimensional effect and/or the presence of significant elastic distortions in the specimens S2−S4 may be the second possible reason for the increase in the observed peak widths. It is known [22,23], that microdeformation and size of coherent scattering regions can be estimated using the time-of-flight technique applying the following dependence of the width of diffraction peaks on the interplanar spacing

$$(\Delta d)^2 = C_1 + C_2 d^2 + \langle \varepsilon^2 \rangle d^2 + d^4/\langle D \rangle^2. \quad (1)$$

Here d — interplanar spacing, Δd — experimentally observed width of the corresponding diffraction peak, C_1 and C_2 — constants describing the function of the instrumental resolution of the diffractometer (they are determined based on the measurements on a standard specimen, powder
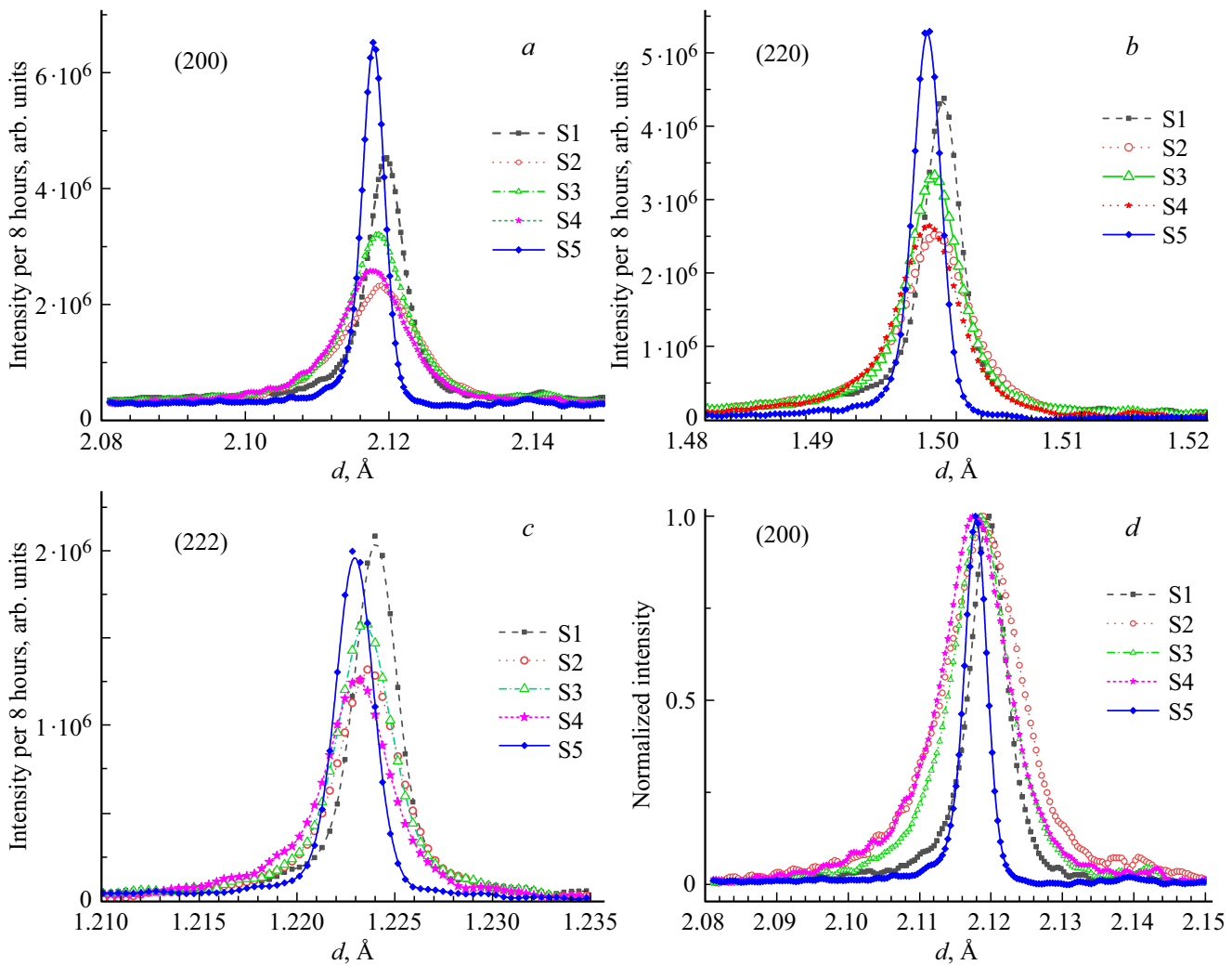

Figure 1. Experimental diffraction patterns (dots) and fitting results (line). Vertical strokes — positions of elastic peaks. The line at the bottom — the discrepancy between the fit and the experiment.

Figure 2. Evolution of the shape of elastic peaks (200) (*a*), (220) (*b*) and (222) (*c*) for specimens S1−S5. Dots — experimental data, lines — result of smoothing procedure. In all the figures, the width of the peaks for S5 practically corresponds to the instrumental resolution. The reflection intensities (200) of specimens S1−S5 are normalized to the maximum of the corresponding distribution in Fig. 2, *d*, for the convenience of comparison. The background is deducted.

Al_2O_3 was used in our case), $\sqrt{\langle \varepsilon^2 \rangle} = (\Delta a / a)$ — dispersion of the parameter a of the lattice cell (microdeformation), $\langle D \rangle$ — average size of coherent scattering regions (CSR). It is easy to see from formula (1) that the last term will play a major role in the effect of broadening of elastic reflections in case of large d and small CSR size D. We obtained the following estimates of the values of the average CSR sizes for specimens S1−S4 using this approach, as well as the results of processing diffractograms (Table 3). The CSR size cannot be determined for S5, i.e. nanostructuring is not observed in it. Since the tenorite phase is released directly from the ESO specimens on cooling, this, of course, causes micro-deformations, but their contribution was not estimated in this work, since additional studies are needed to collect sufficient statistics in the field of small interplanar spacing.

Next, let's try to answer the question „Why is the tenorite phase not observed in neutron diffraction experi-

Table 3. Average size of coherent scattering regions (CSR) of ESO specimens S1−S4 at room temperature

Specimen	S1	S2	S3	S4
CSR Size	≥ 110(6) nm	37(3) nm	48(3) nm	44(3) nm

ments with S2−S4 specimens?". The simulation showed that the most intense peak of the tenorite structure is the reflection (111) with $d = 2.3226$ Å. We analyzed the background in detail in the place where this reflex should be on the diffraction pattern and found a very weak and very blurred peak there. Fig. 3, *a* shows the region of diffraction patterns obtained in the experiment, in which the reflex (111) is still present for specimens S2−S4, and it also shows the simulated peak shape (111) taking into account the resolution function of the diffractometer
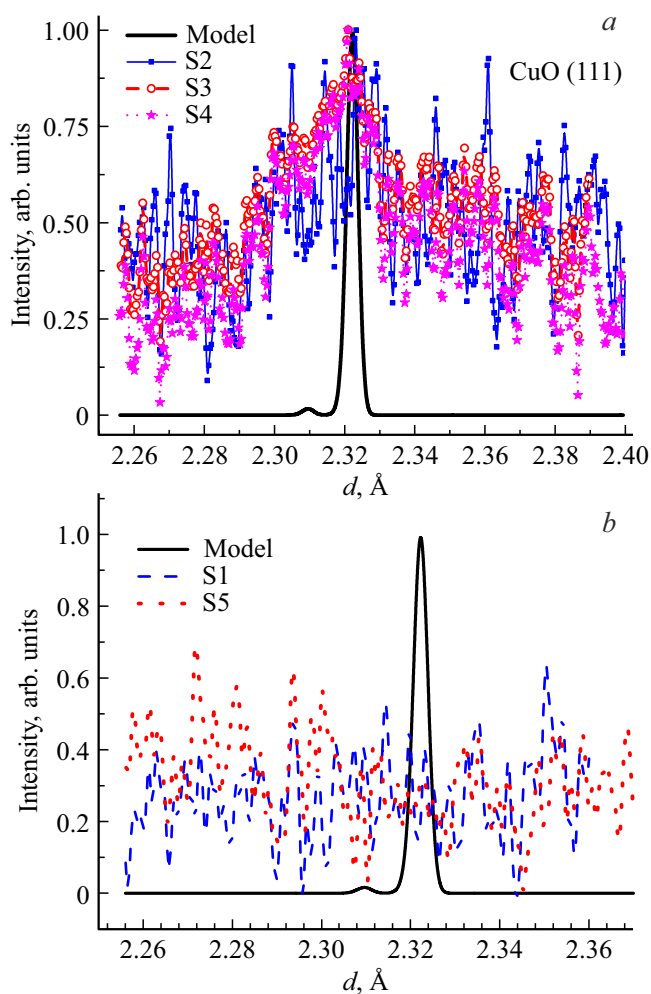
Figure 3. *a* — experimental diffraction patterns in the area of expected observation of elastic peak (111) from the tenorite structure of specimens S2 (blue squares), S3 (red circles) and S4 (lilac stars). Solid black line — the result of neutronogram simulation in the reflex region (111) taking into account the resolution of the instrument. The weak peak on the left on this line is the reflection (200). *b* is the intensity distribution on diffraction patterns in the same region of interplanar spacing of specimens S1 and S5.

(nearby there is and a weak peak (200) from the same tenorite structure). Also for comparison, Fig. 3, *b* shows the intensity distribution in the same region for specimens S1 and S5, where the tenorite phase is not observed in X-ray structural studies. The general background is subtracted and all spectra are normalized to the corresponding maximum intensity in Fig. 3, *a* for convenience of comparison. It is clearly seen that this peak becomes more pronounced and observable with an increase of the percentage of CuO released on cooling at the transition from S2 to S4. The available statistics do not allow for a confident determination of the size of the formed copper oxide nanoparticles for the specimen S2, but it is already sufficient to estimate the size of the CSR in the case of ESO S3

and S4. Using the formula (1) and assuming that the contribution from possible deformations can be neglected, we calculated the values of the average CSR sizes, which turned out to be equal to 168(9) Å and 159(8) Å for S3 and S4, respectively. This coincides well with the estimates given in the article [24], which showed the existence of thread-like CuO nanostructures with similar characteristic sizes in specimens subjected to the same heat treatment as the specimen S3 in our case. It can also be seen from Fig. 3, *a* that for specimen S2 these values can be considered as a sufficiently adequate estimate of the size of CuO nanoparticles formed in it.

4. Conclusion

Studies of the evolution of the crystal structure of ESO (MgNiCoCuZn)O specimens prepared at different cooling rates from synthesis temperature to room temperature, conducted using a high-resolution neutron Fourier diffractometer, showed that a sharp increase of the width of elastic peaks is observed in the case of slow cooling in the furnace (at a rate of 1, 2 and 5 K/min). At the same time, there is no distortion, in particular any peak shape asymmetry, i.e. the rhombohedral and/or tetragonal distortions of the ESO crystal structure expected due to the possible Jan-Teller effect associated with the presence of Cu^{2+} atoms in the octahedral environment were not observed in the experiment. The increase of the widths of elastic reflexes in specimens S2−S4 was primarily caused by the nanostructuring of both the main ESO matrix and the tenorite (copper oxide) released from it on cooling as an additional phase. The characteristic sizes of nanoparticles formed during cooling both in the main ESO phase and in the tenorite phase were determined.

Conflict of interest

The authors declare that they have no conflict of interest.

References

[1] J.W. Yeh, S.K. Chen, S.J. Lin, J.Y. Gan, T.S. Chin, T.T. Shun, C.H. Tsai, S.Y Chang:. Adv. Eng. Mater. **6**, 299 (2004).

[2] J.-W. Yeh, Y.-L. Chen, S.-J. Lin, S-K. Chen. Mater. Sci. Forum **560**, 1 (2007).

[3] M. J.R. Haché, C. Cheng, Y. Zou. J. Mater. Res. **35**, *8*, 1051 (2020).

[4] E.P. George, D. Raabe, R. O. Ritchie. Nature Rev. Mater. **4**, 515 (2019).

[5] C.M. Rost, E. Sachet, T. Borman, A. Moballegh, E.C. Dickey, D. Hou, J. L. Jones, S. Curtarolo, J.-P. Maria. Nature Commun. **6**, art. #8485 (2015).

[6] M. Fracchia, M. Coduri, M. Manzoli, P. Ghigna, U.A. Tamburini. Nature Commun. **13**, art. # 2977 (2022).

[7] E. Castle, T. Csanádi, S. Grasso, J. Dusza, M. Reece. Sci. Rep. **8**, 8609 (2018).

[8] R.-Z. Zhang, F. Gucci, H. Zhu, K. Chen, M. J. Reece. Inorg. Chem. **57**, 13027 (2018).

[9] T. Jin, X. Sang, R.R. Unocic, R.T. Kinch, X. Liu, J. Hu, H. Liu, S. Dai. Adv. Mater. **30**, 1707512 (2018).

[10] J. Gild, Y. Zhang, T. Harrington, S. Jiang, T. Hu, M.C. Quinn, W.M. Mellor, N. Zhou, K. Vecchio, J. Luo. Sci. Rep. **6**, 37946 (2016).

[11] D. Bérardan, S. Franger, D. Dragoe, A.K. Meena, N. Dragoe. Phys. Status Solidi RRL **10**, *4*, 328 (2016).

[12] H. Chen, J. Fu, P. Zhang, H. Peng, C.W. Abney, K. Jie, X. Liu, M. Chi, S. Dai. J. Mater. Chem. A, **6**, 11129 (2018).

[13] B. Li, H. Yang, C. Li, X. He, Y. Zhang. J. Eur. Cer. Soc. **43**, 3437 (2023).

[14] D. Berardan, S. Franger, A.K. Meena, N. Dragoe, J. Mater. Chem. A **4**, 9536 (2016).

[15] S. Zhai, J. Rojas, N. Ahlborg, K. Lim, M. F. Toney, H. Jin, W.C. Chueh, A. Majumdar. Energy Environ. Sci. **11**, 2172 (2018).

[16] R. Liu, H. Chen, K. Zhao, Y. Qin, B. Jiang, T. Zhang, G. Sha, X. Shi, C. Uher, W. Zhang, L. Chen. Adv. Mater. **29**, 1702712 (2017).

[17] D. Berardan, A.K. Meena, S. Franger, C. Herrero, N. Dragoe. J. Alloys Comp. **704**, 693 (2017).

[18] Zs. Rák, J-P. Maria, D.W. Brenner. Mater. Lett. **217**, 300 (2018).

[19] A.M. Balagurov. Neutron News **16**, 8 (2005).

[20] A. Balagurov, D. Balagurov, I. Bobrikov, A. Bogdzel, V. Drozdov, A. Kirilov, V. Kruglov, S. Kulikov, S. Murashkevich, V. Prikhodko, V. Shvetsov, V. Simkin, A. Sirotin, N. Zernin, V. Zhuravlev. Nucl. Instr. Meth. Phys. Res. B **436**, 263 (2018).

[21] V. Nallathambi, L.K. Bhaskar, D. Wang, A.A. Naberezhnov, S.V. Sumnikov, E. Ionescu, R. Kumar. J. Eur. Cer. Soc. **43**, *10*, 4517 (2023).

[22] G.D. Bokuchava, R.N. Vasin, I.V. Papushkin. Surface. Poverkhnost'. Rentgenovskie, sinkhrotronnye i neytronnye issledovaniya **5**, 3 (2015). (in Russian).

[23] G.D. Bokuchava, I.V. Papushkin, V.I. Bobrovsky, N.V. Kataeva. Poverkhnost'. Rentgenovskie, sinkhrotronnye i neytronnye issledovaniya **1**, 49 (2015). (in Russian).

[24] D.R. Diercks, G. Brennecka, B.P. Gorman, C.M. Rost, J.-P. Maria. Microsc. Microanal. **23**, *1*, 1640 (2017).

Translated by A.Akhtyamov